Optimisation of Trailing Edge Flaps on the Base Cavity of a Vehicle for
Improved Performance at Yaw

N.B. When citing this work, cite the original published paper.

(article starts on next page)

Optimisation of Trailing Edge Flaps on the Base Cavity of a Vehicle for Improved Performance at Yaw

Magnus Urquhart[1] · Simone Sebben[1]

© The Author(s) 2022

Abstract

Regulations to reduce greenhouse gas emissions of passenger vehicles are becoming increasingly stringent. The aerodynamic drag is a major contributor to the vehicle's total energy consumption where a large portion is attributed to the base wake. This paper optimises the angles of small trailing edge flaps on a base cavity of a full-scale sports utility vehicle placed in a wind tunnel. The trailing edge flaps are controlled using servos mounted inside the cavity. The flap angles are optimised using a surrogate model based optimisation algorithm with the objective of reducing the aerodynamic drag at different yaw angles and to create a yaw-insensitive geometry by considering several weighted yaw angles to form the driving cycle averaged drag. Low drag designs are further investigated using base pressures and wake measurements. The results show that the base pressures are symmetrised by reducing the crossflow in the wake. As the model is yawed the wake becomes increasingly downwash dominated by a large rotating windward structure which is reduced by the optimised flaps. The cycle averaged drag optimised design has a smaller increase in drag when yawed compared to a design optimised without considering yaw.

1 Introduction

There is a global strive towards more energy-efficient vehicles where regulations and electric vehicle range are driving factors. The aerodynamic drag accounts for more than a quarter of the traction energy required (Pavlovic et al. 2016). Road vehicles are short blunt bodies with massively separated wakes where the pressure drag accounts for approximately 90% of the total aerodynamic drag (Schuetz 2015). Because of this, a lot of focus has been placed on reducing the pressure difference between front and rearward facing surfaces mainly by increasing the base pressure.

✉ Magnus Urquhart
magnus.urquhart@volvocars.com

Simone Sebben
simone.sebben@chalmers.se

[1] Mechanics and Maritime Sciences, Chalmers University of Technology, Hörsalsvägen 7B, 41258 Gothenburg, Västra Götaland, Sweden

This work applies a tapered cavity to a full-scale SUV. Tapering alone is an effective drag reduction technique showing up to 20% reduction in drag (Howell et al. 2013; Ahmed et al. 1984; Varney et al. 2018). Cavities are also known to be an efficient method of drag reduction both with and without yawed flow (Evrard et al. 2016; Duell and George 1993; Bonnavion et al. 2019; Varney 2020). The combination of both methods reduces the drag further (Cooper 1985).

There are several on-road effects that influence aerodynamic drag such as wind, traffic and cornering (Favre and Efraimsson 2011; Tunay et al. 2018; Le Good et al. 2018; Josefsson et al. 2018). Constant side wind has been shown to produce a non-linear drag rise depending on the vehicle shape (Howell 2015) and significantly influence the wake topology (Rao et al. 2019). Windsor (2014) investigated 51 passenger vehicles and found that the sensitivity to yaw was generally higher for vehicles with low drag at 0°-yaw. This highlights the need to consider several operating conditions to achieve real-world reductions for highly optimised vehicles.

Howell et al. (2018) introduced a driving cycle equivalent drag measure for this purpose which takes into account the wind distribution and driving cycle to generate a representative aerodynamic performance figure. An engineering estimate of the cycle averaged drag was also introduced which can be used at a lower cost during vehicle development.

Bluff body wakes continue to be an actively researched area primarily focused on wake flow without yaw, however, several studies at yaw exist (Howell 2015; Windsor 2014; Cooper 2003; Sterken et al. 2014a; Favre 2011; Pfeiffer and King 2018; Li et al. 2019; Lorite-Díez et al. 2020). The literature is often limited to symmetric designs, although asymmetric tapering was investigated by Garcia de la Cruz et al. (2017) and Varney et al. (2018), showing drag reductions over symmetric designs when the windward side was tapered more than the leeward side. Similar results were found by Li et al. (2019) who applied pulsed jets to the sides of an Ahmed body at yaw and found a reduction in drag by deviating the windward shear layer towards the leeward side.

Recently, Urquhart et al. (2020a) optimised the angles of flaps applied to the trailing edge of a tapered cavity using a generic model-scale vehicle. Nine flaps were used, three on each of the sides and three on the roof. The results showed that both laterally and vertically asymmetric designs can lower drag by improving the wake symmetry, reducing the crossflow in the recirculating region. The flap angles were limited to positive, or outward, angles only and no flaps were applied to the floor. This work extends the scope of trailing edge flaps on a tapered base cavity to include negative angles and flaps on the floor on detailed production geometry at a full scale Reynolds number. Further, the flaps are optimised to create a static symmetric geometry where the cycle averaged drag is used as the objective function.

2 Methodology

2.1 Test Object with Flaps

The test object is a full-scale Volvo XC40 recharge SUV electric vehicle with an added base cavity extending the geometry by approximately 150–200mm, or 5% of the vehicle length. This results in a cavity with different longitudinal position around the perimeter, maintaining the SUV shape. The trailing edge is fitted with 12 flaps that are 80mm long, or 2% of the vehicle length, extending the cavity, Fig. 1a. The flaps are 5mm thick with
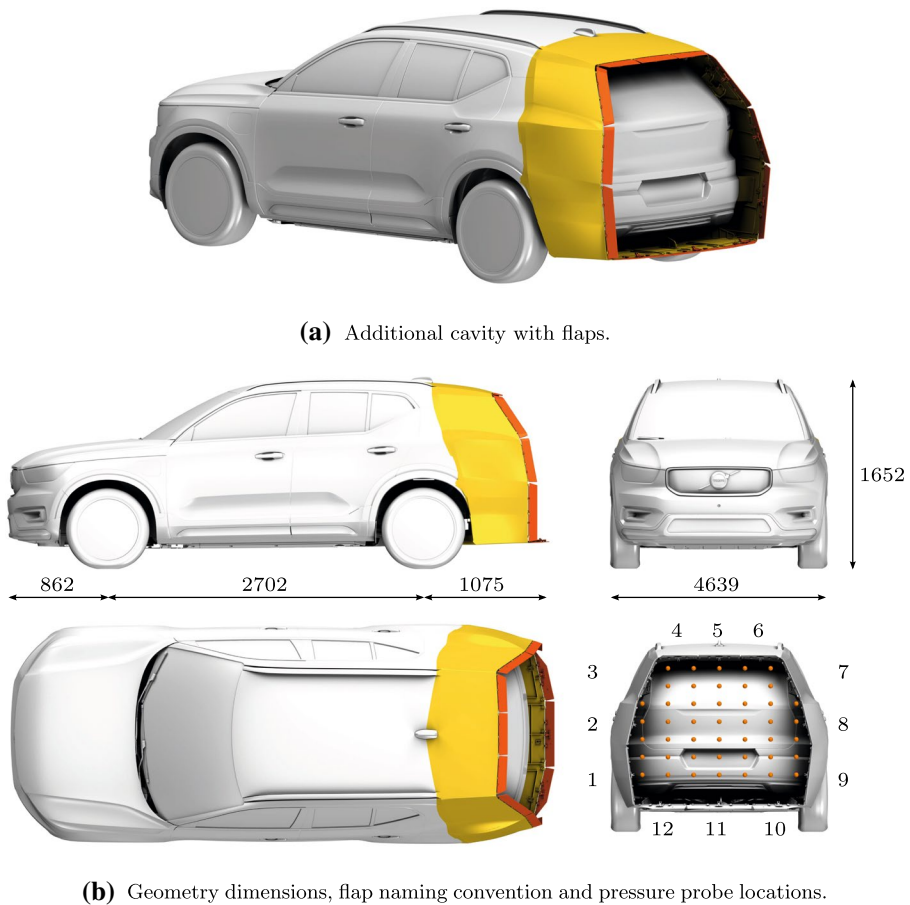
(a) Additional cavity with flaps.

(b) Geometry dimensions, flap naming convention and pressure probe locations.

Fig. 1 Volvo XC40 recharge geometry

a radius of 2.5mm around the perimeter. The cavity walls are 5mm thick with additional strengthening at the mounting points as well as ribs to increase the panel stiffness. The cooling inlets at the front of the vehicle are closed and the rearview mirrors are removed from the model. Covers are also placed on the rims. These changes create a baseline with good flow to the rear of the vehicle and low drag which highlights the potential of the flaps as well as being representative of future vehicles with rearview cameras, low drag rims and actively controlled cooling inlets. The bottom of the cavity is aligned tangent at the same height as the flat floor. The cavity provides additional tapering resulting in an approximately 15° taper on the sides and roof with no tapering on the bottom which is similar to other geometries with base cavities at yaw (Lorite-Díez et al. 2020; Garcia de la Cruz et al. 2017; Urquhart et al. 2020a, 2018). Figure 1b shows the pressure tap locations on the base and the clockwise flap naming convention.

The flap angles are defined relative to the existing tapering where a positive angle denotes the flap moving outwards, towards the freestream. The flaps can move ±25° using Dynamixel XL430-W250-T servos connected with linkages and horns resulting in a 1:1 ratio between the servo arm and flap movement. The servos have a stall torque of 1.4Nm.

The flap positions were controlled using an Arduino Mega with a Dynamixel shield and an Xbee PRO S1 allowing the flaps to be controlled wirelessly from the control room outside of the test section. This automated process enables more designs to be tested in a given amount of time as the wind tunnel can be kept running while continuously changing designs. The position of each servo is automatically checked before sampling to ensure that the angle signal has reached and correctly mapped the set point before sampling the design performance. The flaps are held at the set point throughout the test by keeping the torque on to ensure that the position is maintained during the sampling period. No movement of the flaps was observed due to the aerodynamic forces throughout the test.

Evaluating one design takes approximately 1 min and 30 seconds from the time the design request is sent to the time the result is saved. Because the wind is on continuously, the flaps are first all set to the −25° degree position. This is expected to be the least favourable position as the total flap angle to the freestream is approximately 40° on the sides and roof. This is done to reduce any hysteresis effects where the current design performance is dependent on the previous design as the angle which the flow separates is often greater than the angle the flow reattaches. After 10 seconds at the −25° degree position, the flaps are set to the desired angles. Once the flaps are in position, the flow is allowed to develop for 10 seconds after which a 20 second average of the forces is taken.

The repeatability of the method was evaluated by testing a design where all flaps are set to 0° 20 times. The repeatability for a 95% confidence interval was calculated to $\pm C_D = 0.0008$ at 0°-yaw.

The flaps were limited to 2° increments to reduce excessive testing of similar designs and promote exploration of the designs space. Even though the design space is limited, it is still large in the context with $26^{12} = 9.54 \times 10^{16}$ possible design combinations. Sampling all possible designs for one yaw angle would take approximately 300 billion years. This highlighting the need for efficient optimisation methods when working with large a design space.

2.2 Test Facility

The wind tunnel experiments were performed at the Volvo Cars Aerodynamic Wind Tunnel (PVT) which is capable of speeds of up to 250 km/h. In this work, the tests were done at 100km/h, resulting in a Reynolds number of $Re_{\sqrt{A}} = 3.1 \times 10^6$ based on the square root of the vehicle frontal area, A. The tunnel is of closed return type with slotted walls with a test section of $27\,\text{m}^2$ resulting in a blockage ratio of approximately 10% for a full-scale geometry.

The ground simulation consists of a five belt moving ground system mounted with boundary layer control consisting of a scoop followed by a distributed suction. There are tangential blowers behind each belt to extend the apparent length of the belts. The vehicle is mounted on a turntable to allow yawing of the model. A positive yaw angle is denoted with the nose pointing right following the SAE standard J1594 [28]. In the presented study, only positive yaw angles are used, i.e. the wind moves from left to right when looking at the vehicle from the rear. The vehicle is connected to a six-component balance using four struts which fixate the vehicle's position and height. The use of a full-scale wind tunnel and vehicle model allows for realistic Reynolds numbers and rotating wheels with ground simulation, besides allowing for easier manufacturing and maintenance of the flaps and servos.

The forces and moments are non-dimensionalized to coefficients and corrected for blockage effects. The reported repeatability within the same test without removal of the

model is $C_D = \pm0.001$ for a 20 second average and the tunnel is accredited according to the European Accreditation procedure EA 4/02 (Sternéus et al. 2007). The average velocity varies within 0.05km/h for one test. The reported repeatability is outside that of the previously calculated interval for flap movement of $C_D = \pm0.0008$.

Base pressures were measured using a PSI ESP-64HD 64 channel pressure scanner where each measurement was averaged for 20s. The pressure spades are mounted on top of aluminium tape to provide a good bond between the aluminium tape and the probe. All pressure tubes are mounted flush and exit the cavity behind the right rear wheel to minimise any influence on the flow. A traversing unit was used to capture the wake flow featuring two 12-hole pressure probes, or omniprobes, mounted 56mm apart vertically and were swept with a 112mm vertical spacing. The probes are capable of capturing flow within $\pm150°$ (Aeroprobe 2018) and were placed at a 45° angle to better capture the reversing flow in the wake. Measurements taken with a traversing unit are known to be intrusive, influencing the flow and vehicle drag (Sterken et al. 2014b). The results from Sterken et al. (2014b) indicate that the global wake structures are qualitatively similar with and without the traversing unit. The mounted vehicle along with the traversing unit is shown in Fig. 2. More information on the wind tunnel can be found in (Sternéus et al. 2007; Ljungskog 2019).

2.3 Optimisation

A surrogate model-based optimisation algorithm developed in previous work for aerodynamic optimisation (Urquhart et al. 2020a) is used. Surrogate model-based algorithms are particularly useful when the number of affordable function evaluations is small, typically less than 1000.

The surrogate model is built from an initial set of designs created using a Latin Hypercube (LHC) sampling plan. The Latin Hypercube sampling plan divides each design parameter into n equally sized intervals where n is the number of designs in the plan. The same value for a given design parameter can only occur once which ensures even coverage for each design dimension. The distance between each sample is optimised to reduce clustering and increase the coverage between each dimension within the sampling plan. The inter-sample distance is optimised using a genetic optimisation algorithm based on the work by Bates et al. (2004). Figure 3 shows an example of an optimised plan with 100 points in two design dimensions.

Fig. 2 Volvo wind tunnel experimental setup

Fig. 3 Example of Latin Hyper-
cube sampling plan containing
100 points
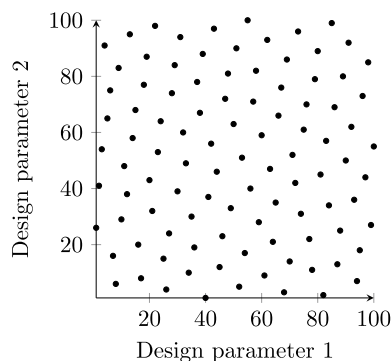
The surrogate model is based on Radial Basis Function (RBF) interpolation. The RBF interpolant is analogous to a neural network with a single layer. The basis function combines the inputs linearly as

$$u(\mathbf{x}) = \sum_{i=1}^{N} w_i \xi_i(\|\mathbf{x} - \mathbf{x_i}\|_2) \tag{1}$$

where $u(\mathbf{x})$ is the surrogate prediction, w_i are the weights, ξ_i is the Radial Basis Function, N is the number of sampled designs and $\|\mathbf{x} - \mathbf{x_i}\|_2$ denotes the Euclidean distance between the evaluated design $\mathbf{x}$ and the i-th design $\mathbf{x_i}$.

The weights w_i are solved exactly by solving the linear system

$$\mathbf{Aw} = \mathbf{u} \tag{2}$$

where $\mathbf{A} = A_{ij} = \xi_i(\|x_i - x_j\|_2)$ and $\mathbf{u} = \mathbf{u}(\mathbf{x_i})$ are the objective function values for each sample. An additional regression term, λ, is added to the diagonal of $\mathbf{A}$, Equation (2). This term relaxes the requirements of the surrogate model being strictly interpolating, this is particularly useful when optimising experimental functions or functions containing noise in general as this removes unwanted high-frequency oscillations. Radial Basis Functions can exhibit poor performance if the scale between the input to output differs greatly between dimensions. To solve this, each design parameter is normalised and scaled with a linear scaling factor c_j.

Three RBFs, ξ_i, are used in the surrogate model to increase the flexibility of the model during training. These are the gaussian, $\xi(r) = e^{-(\varepsilon r)^2}$, inverse quadratic, $\xi(r) = \frac{1}{1+(\varepsilon r)^2}$ and inverse multiquadratic, $\xi(r) = \frac{1}{\sqrt{1+(\varepsilon r)^2}}$ where ε is the width factor of each RBF.

The ridge regression term, λ, widths, ε, Radial Basis Function ξ_i and axis scaling c_j are all hyperparameters of the surrogate model and are optimised using a leave-one-out objective function to improve the prediction performance. The leave-one-out objective function creates the surrogate with all but one design which is used to evaluate the accuracy. This process is repeated for all designs and the root mean squared error of all points is the leave-one-out objective function. The equivalent structure of the surrogate model is shown in Fig. 4.

Training of the surrogate model hyperparameters is done using Differential Evolution which is a stochastic optimisation algorithm. This results in the surrogate model creation being stochastic and different models are obtained each time the model is trained even when using the same input data. The stochastic property is used to improve the

Fig. 4 Radial Basis Function surrogate model network structure

input layer   scaling layer   hidden layer   output
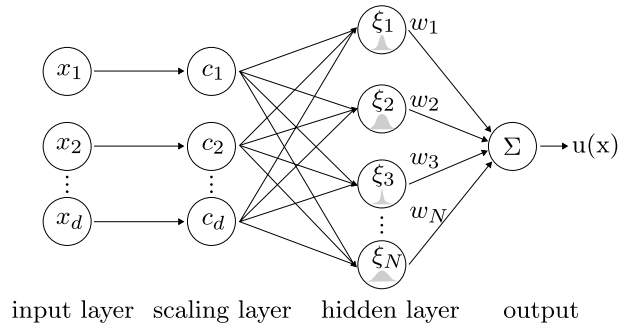
optimisation process by training several models using the same data. The median of the ensemble of models is used as the function value prediction and the standard deviation between the models is used as an estimate of the surrogate model uncertainty. The optimisation process then samples designs that both explore the design space, reducing the model uncertainty, and exploits the current knowledge, reducing the function value.

The surrogate model performance, in terms of reduction in objective function value per function evaluation, was compared with other commonly used optimisation algorithms, Random Sample, Differential Evolution, Nelder-Mead and Bayesian Optimisation. Nine different benchmark problems were investigated where each function was evaluated with and without added random noise. Each benchmark problem was repeated a minimum of 100 times for each algorithm to gather statistics. The surrogate model outperformed, or performed as good as the other algorithms, in 17 out of the 18, being in close second position for the remaining problem (Urquhart et al. 2020b).

The flap angles are optimised separately for 0°, 5° and 10°-yaw. Additionally, a cycle averaged drag formulation is used to create a yaw-insensitive design to reduce real-world consumption. Howell et al. (2017) proposed the cycle averaged drag coefficient, C_{DWC}, considering the wind distribution and driving cycle to generate a representative performance figure as well as a simplified engineering estimate of the full cycle averaged drag. Howell et al. (2017) found that C_{DWC} to be 5% higher on average compared to C_D at 0°-yaw with the smallest and largest difference being 2.2% and 11.4%, respectively.

Varney et al. (2018) used the engineering estimate of the cycle-averaged drag to study asymmetric side tapering. The cycle averaged drag was further modified by Varney et al. (2018), removing the 15°-yaw term as its contribution is relatively small since the likelihood of large yaw angles reduces faster then the drag increases from increases in yaw. The relative weighting of each yaw angle follows no physical meaning and is found using curve fitting of the full integrated cycle averaged drag. The simplified engineering estimate used throughout this work reads

$$C_{DWC} = 0.53 C_{D0} + 0.345 C_{D5} + 0.13 C_{D10} \qquad (3)$$

where the subscript denotes the yaw angle.

The flap angles were optimised for the cycle averaged drag by running 5–10 designs at one yaw angle before switching yaw angle. A surrogate model for the remaining two angles was used to be able to estimate the cycle averaged drag and perform the optimisation without changing yaw angle for each design. This is a large benefit of surrogate model optimisation as time can be saved by evaluating several designs at one yaw angle before switching yaw angle. This reduces the optimisation effort considerably compared to other algorithms,

e.g. Nelder-Mead, where the full cycle averaged drag needs to be tested for each successive iteration. After 5–10 designs the model is yawed and the designs which were estimated by the surrogate model are instead explicitly tested.

3 Results and Discussion

The geometry is optimised for 0°, 5° and 10°-yaw as well as for the cycle averaged drag, Equation (3). First the optimisation results are presented followed by detailed analysis at 0° -yaw and then at yaw.

3.1 Optimisation

The optimisation is limited to only laterally symmetric designs for the entire optimisation period at 0°-yaw where 280 designs were tested. The symmetry constraint is expected to increase the convergence speed and generate designs that perform well while significantly limiting the available design space. First, the optimisation is performed on a subset of the entire design region where each side of the model is forced to take on the same angle. Afterwards, 20 additional LHC samples are added and the optimisation is continued in the full design space while maintaining the knowledge gathered in the constrained design space. The same procedure is performed at yaw, however, then the design is not limited to being laterally symmetric.

There were no fixed criteria for the cutoff point when the optimisation was switched from the constrained to the full design space. Neither was there a specific criterion for when the optimisation process was stopped due to the vastness of the design space. This was done when it was deemed that no further significant improvement to the objective function could be achieved, based on the convergence history as well as the surrogate model prediction accuracy and was monitored throughout the optimisation process. In this work, each objective was optimised once due to the available resources. Performing the same optimisation several times would increase the confidence in the found optimum design.

The optimisation history at 0°-yaw is shown in Fig. 5 where the error bars indicate the repeatability interval. The largest reductions are found early in the optimisation routine. However, due to the vast design space, additional iterations were carried out, improving the prediction accuracy of the surrogate model as more data was added. An improvement
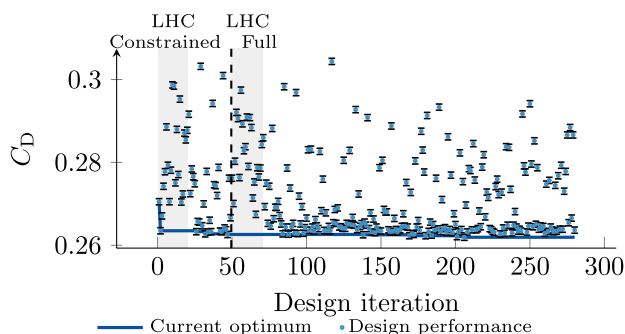

Fig. 5 Flap optimisation history at 0°-yaw. Error bars indicate the 95% confidence interval

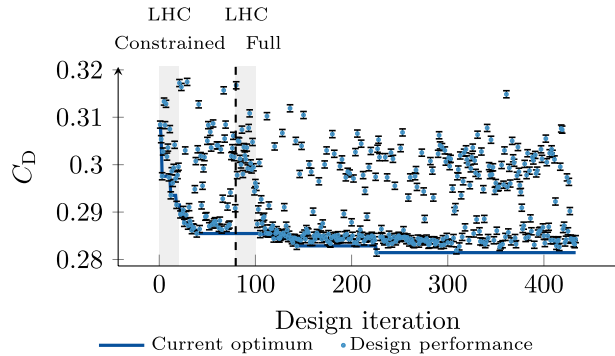**Fig. 6** Flap optimisation history at 5°-yaw. Error bars indicate the 95% confidence interval

Table 1 Aerodynamic force coefficients at 0°-yaw

Configuration.	C_D	C_{FL}	C_{RL}	C_{DB}
Smooth cav.	0.280	0.027	0.137	0.088
0°-yaw opt.	0.263	0.023	0.081	0.069
Cycle ave. opt.	0.267	0.023	0.070	0.071

greater than the repeatability interval could not be found in the full design space compared to the constrained space.

The 5° and 10°-yaw optimised designs were run for 433 and 206 iterations respectively. The optimisation history for 5°-yaw is shown in Fig. 6, with a similar history observed at 10°-yaw. Significant improvement in the full design space was found for the yawed designs which was not the case at 0°-yaw.

The cycle averaged drag optimised design used the information gathered from the 0° -yaw optimisation. In total 335, 245, 266 symmetric designs were tested at 0°-yaw, 5°-yaw and 10°-yaw, respectively, where 55 different cycle averaged designs were tested explicitly. For the yawed cases, an additional 20 designs were added to explore the design space.

First, the symmetric designs are presented at 0°-yaw flow condition. The symmetric designs are the smooth cavity (all flaps set to 0°), the flaps optimised for 0°-yaw drag and the cycle averaged drag optimised design. Then the results at yaw are presented and discussed where the three symmetric geometries are shown as well as two additional asymmetric designs optimised for 5°-yaw and 10°-yaw respectively.

3.2 0°-Yaw

Only the best designs are presented and investigated further, however, several designs with similar performance, within the 95% repeatability interval are found. The force coefficients are presented in Table 1 where the subscripts FL and RL denote front lift and rear lift and DB is the integrated base drag coefficient from the pressure measurement. Predictably, the geometry optimised for 0°-yaw has the lowest drag, approximately 20% lower than the production vehicle. A design where all flaps are set to 0° was also tested for comparison and is referred to as a smooth cavity.

Figure 7 shows the base pressure distributions for the smooth cavity, the 0°-yaw optimised geometry as well as the cycle averaged drag optimised configuration. A slight
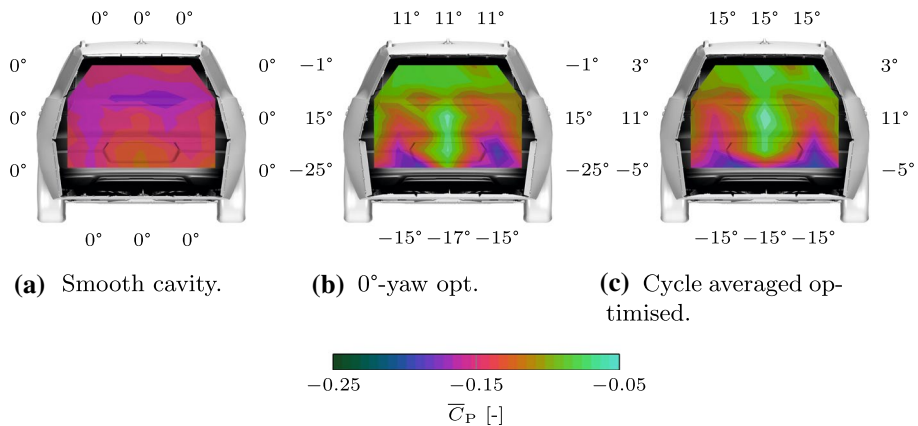
Fig. 7 Base pressure at 0°-yaw

asymmetry can be seen in the base pressures. There are some asymmetries in the underbody of the vehicle which can cause the shift in base pressures. Cavities of this length and greater can suppress long term wake dynamics such as bi-stable behaviour Varney (2020). Capturing the base pressure twice with the same geometry only revealed minor differences and no qualitative changes could be seen. The pressure distribution for the smooth cavity with a high value towards the bumper is consistent with a wake that is downwash dominated which can be seen in the crossflow wake plane, Fig. 8, where the crossflow, $\overline{V}_{yz\ magnitude}$, is defined as the magnitude of the vertical and lateral velocity components. The 0°-yaw optimised geometry has a centrally located high-pressure region and shows no obvious bias towards an upwash or downwash dominated wake. This is an expected result as a balanced wake has been linked with low drag (Varney 2020; Urquhart et al. 2020a, [36], Wang et al. 2020). The cycle averaged drag optimised design results in an upwash biased wake with a slightly higher drag compared to the 0° -yaw optimised geometry.
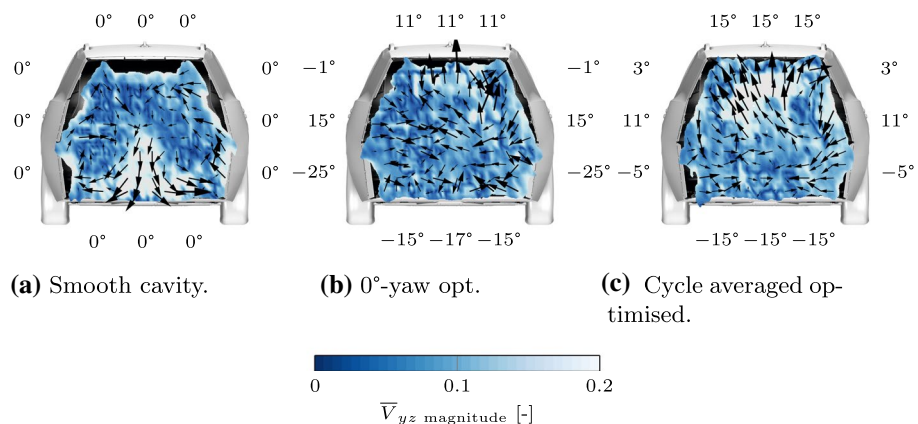

Fig. 8 Crossflow velocity magnitude, $\overline{V}_{yz\ magnitude}$, at 7% of the vehicle length behind the vehicle at 0°-yaw. The values are normalised by V_∞ and clipped where the total pressure coefficient is larger than 0

Based on the crossflow, Fig. 8, it is not obvious that the cycle averaged optimised geometry has significantly less drag than the smooth cavity. However, the drag difference is evident in the base pressures. Further analysis including a centreline plane would be beneficial and could highlight any differences in wake balance close to the wake, however, no centreline planes were measured. Due to the slanted rear window, an upwash biased wake may have lower drag than a downwash biased wake, this observation would require further investigation.

The flaps behind the wheels, flaps 1 and 9, are significantly different for the 0°-yaw optimised and cycle averaged drag optimised design. The cycle averaged drag optimised flaps are close to the existing tapering. The difference likely stems from the flow being separated in this region resulting in very low sensitivity of the flap position when the optimisation is performed at 0°-yaw. Many modern vehicles feature bumpers with highly rounded corners, this could be an artefact of designing vehicles primarily at 0°-yaw.

Several designs in the optimisation process featured similar drag values with a large difference in flap angles, particularly on the sides. The sensitivity to flap angle changes was investigated locally by modifying the angle of one flap in ±2.5° and ±5° increments. At 0°-yaw, the designs are symmetric and the same constraint is applied for the sensitivity analysis. Changes in drag that are smaller than the 95% repeatability interval are greyed out. Figure 9 shows the sensitivity analysis for the 0°-yaw optimised design. There are mainly increases in drag around the 0°-yaw optimised design which is expected when a local optimum is found. The roof flaps located at the sides, flaps 4 and 6, are the most sensitive to changes. Flap 5 does not show the same high increase in drag for a 5° reduction in flap angle. This flap is located at the top centre of the geometry and due to the symmetry constraint, has less area than flaps 4 and 6 which are moved in unison.

3.3 5° & 10°-Yaw

It is primarily the results at 5°-yaw which are presented in this section as the 10°-yaw results are similar.

Table 2 shows the drag values for the tested yaw angles as well as the cycle averaged drag. The 5° and 10°-yaw optimised geometries are listed as "Active opt." as these designs require movement to actively adapt to the current wind conditions. The 95% repeatability interval for the cycle averaged drag values is also shown since the uncertainty is reduced when combining three weighted values. The repeatability for the other designs remains the
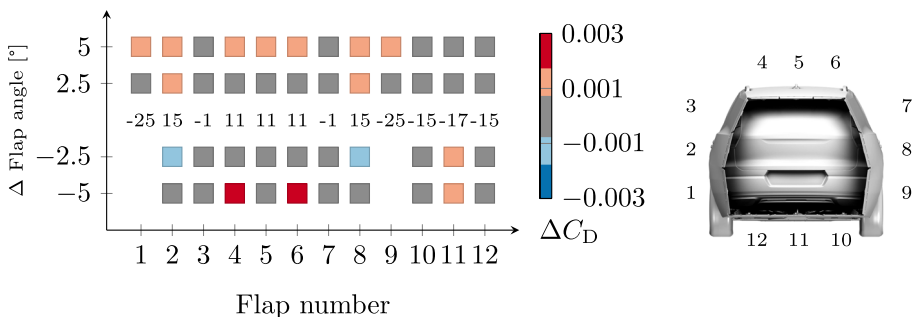

Fig. 9 0°-yaw optimised design sensitivity to flap angle changes of each flap while keeping the other flap angles constant at the best design found (left). Flap naming convention (right)

| Table 2 Aerodynamic force coefficients. The repeatability interval is $\pm C_D = 0.0008$ for the single measurements	Configuration.	$C_{D,0}$	$C_{D,5}$	$C_{D,10}$	C_{DWC}
	Smooth cav.	0.280	0.298	0.338	0.2952 ± 0.0005
	0°-yaw opt.	0.263	0.296	0.334	0.2849 ± 0.0005
	Active opt.	0.263	0.286	0.325	0.2803 ± 0.0005
	Cycle ave. opt.	0.267	0.292	0.330	0.2852 ± 0.0005

same ($\pm C_D = 0.0008$). The cycle averaged drag values for the 0°-yaw and the cycle averaged drag optimised geometry is within the uncertainty margin.

the base pressure distribution for the symmetric designs are qualitatively similar, Fig. 10a, b and d. There is a high-pressure zone on the windward side of the model biased to the lower part of the vehicle. This is shifted upward for the cycle averaged optimised design compared to the other two symmetric designs, resulting in overall higher base pressure. The high-pressure bias toward the lower part of the wake suggests that it is a primarily downwash dominated wake.

The 5°-yaw optimised design has a more uniform base pressure distribution. The high-pressure zone is located toward the bumper and this likely extends outside of the measure region further down on the bumper, lowering drag compared to the other designs.

Even though the cycle averaged drag values between the cycle averaged drag optimised (0.2852) and 0°-yaw optimised (0.2849) designs are similar, the flap angles are significantly

(a) Smooth cavity.

(b) 0°-yaw opt.

(c) 5°-yaw opt.

(d) Cycle averaged opt.

$\overline{C}_P$ [-]
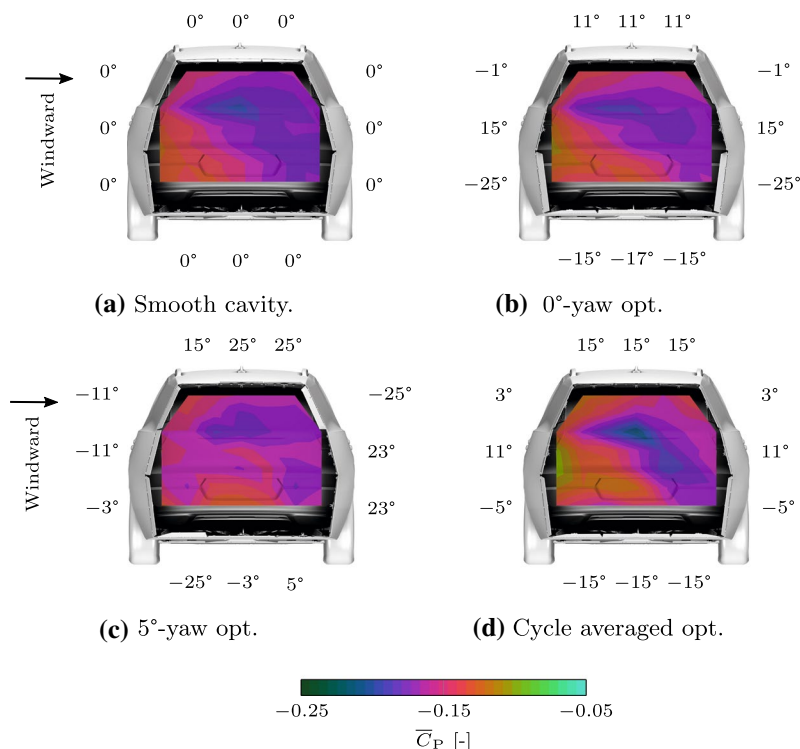
Fig. 10 Base pressure at 5°-yaw

different. It is important to note, however, that a reduction in lift is observed across the yaw sweep. This will be further discussed later in this section.

The symmetric designs were tested for a full yaw sweep from −20° to 20°, Fig. 11. The cycle averaged drag optimised design outperforms the 0°-yaw optimised design at all yaw angles except at 0°-yaw. This is consistent with the observations found by Windsor (2014) where low drag saloon vehicles at 0°-yaw were more likely to have larger drag increases at yaw. It is only at 0°-yaw where the 0°-yaw optimised design outperforms the cycle averaged drag optimised design. The reason for this is further investigated in this section. A large benefit for the cycle averaged optimised design is the reduction in lift over the range, Fig. 11. This improves vehicle stability and safety.

The crossflow for the configurations at 5°-yaw is shown in Fig. 12. At yaw, the plane is measured normal to the tunnel flow while the vehicle is yawed on the turntable. The crossflow magnitude is calculated relative to the vehicle coordinate system. The smooth cavity has a large rotating structure at the top windward portion of the wake. This structure creates a mainly downwash dominated wake as the vehicle is yawed. This is reduced by the 0°-yaw optimised design and further reduced by the cycle averaged drag optimised design. This structure is not evident in the asymmetric, 5°-yaw optimised design, consistent with the 0°-yaw results where low drag was found for balanced wakes with low crossflow. Generally, the flaps are pointing against the wake vectors to cancel out the crossflow in the wake. This is in line with results from previous work optimising flaps on the generic Windsor body at yaw (Urquhart et al. 2020a).

The large scale rotating structure has been identified in previous works at yaw (Urquhart et al. 2020a, 2018; Wieser et al. 2020). These results show that the wake becomes either increasingly upwash or downwash biased as the vehicle is yawed. Howell (2015) showed that the drag increase at yaw is either positively or negatively correlated with the lift change at yaw depending on the vehicle shape. His findings are consistent with a wake becoming either upwash or downwash biased as the vehicle is yawed. The model scale geometry investigated in (Urquhart et al. 2020a) becomes increasingly upwash dominated as the vehicle is yawed and benefits from a reduction in roof flap angle to reduce drag at yaw. The geometry investigated here becomes more downwash dominated at yaw and thus benefits from an increase in the roof flap angle, adding a slight upwash bias to the wake at 0°-yaw, which also reduces lift. The vehicle pitch angle and ground clearance height is also known to influence the wake balance Bonnavion and Cadot (2018). This is an important factor to consider as more vehicles are taking
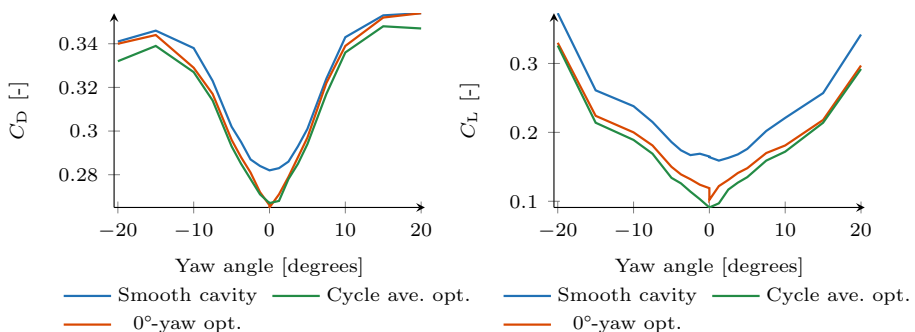

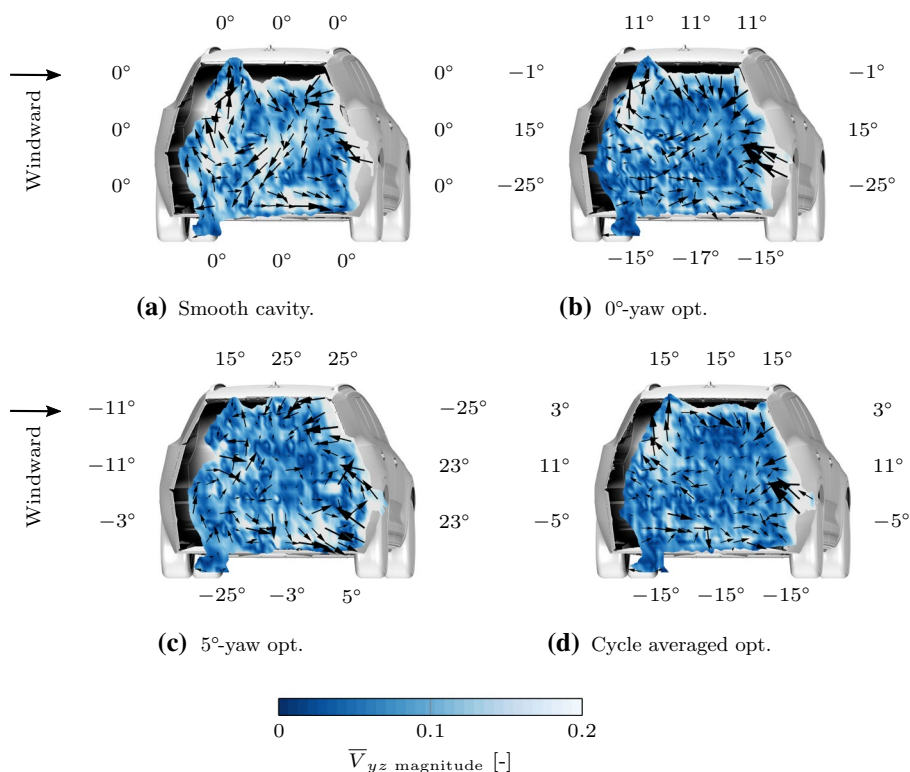**Fig. 11** Yaw sweep of the smooth cavity, 0°-yaw optimised and the cycle averaged drag optimised designs

(a) Smooth cavity.   **(b)** 0°-yaw opt.

(c) 5°-yaw opt.   **(d)** Cycle averaged opt.

$$\overline{V}_{yz \text{ magnitude}} \ [-]$$

Fig. 12 Crossflow velocity magnitude, $\overline{V}_{yz \text{ magnitude}}$, behind the vehicle at 5°-yaw. The values are normalised by V_∞ and clipped where the total pressure coefficient is larger than 0

advantage of active suspension systems to reduce the ride height at high speeds to lower drag. The effectiveness of such a strategy needs to be evaluated considering a cycle averaged performance as it will be influenced by the combined wake balance changes from the active ride height change and yaw.

The reason for the lateral position difference of the large twisting structure between vehicle geometries is not fully understood. Wieser et al. (2020) investigated the generic notchback DrivAer vehicle at yaw and showed a windward vortex originating from the C-pillar. This structure can delay the formation of the large scale rotating structure which moves towards the leeward side of the vehicle, causing it to become increasingly upwash dominated at yaw. The lack of a windward C-pillar vortex for the geometry investigated in this work allows for an early formation of the rotating wake structure which causes the wake to become downwash dominated instead.

This theory is supported by the results from Rossitto et al. (2017) where rounding of the C-pillar was investigated and thus suppressing the C-pillar vortices. The sensitivity to side wind reduced while the rear lift reduced at 10°-yaw. This is not expected for this vehicle type as reductions in lift are correlated with increasing drag sensitivity to side wind based on the results from Howell (2015). Rossitto et al. (2017) results from C-pillar rounding strengthens the theory that the windward vortex originating from the C-pillar, or lack thereof, interacts with the lateral position of the large rotating structure in the wake at yaw.
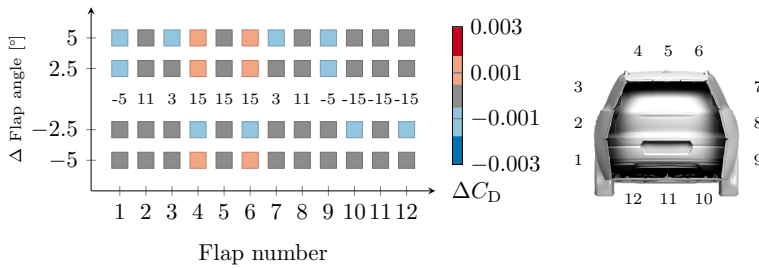
Fig. 13 Cycle averaged drag optimised design sensitivity to flap angle changes of each flap while keeping the other flap angles constant at the best design found (left). Flap naming convention (right)
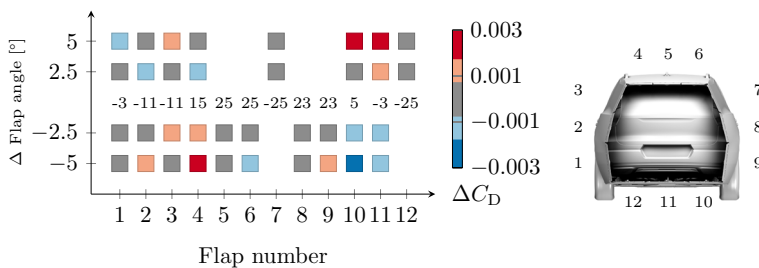

Fig. 14 5°-yaw optimised design sensitivity to flap angle changes of each flap, while keeping the other flap angles constant at the best design found (left). Flap naming convention (right)

The design optimised for 10°-yaw features the same trends as the flap angles for the 5°-yaw optimised design with the flap angles (3°, −13°, 5°, 25°, 25°, 25°, −25°, 25°, 25°, −19°, −25°, −25°). The angles for most flaps has increased with several flaps at their maximum or minimum position. This shows that as the model is yawed, larger actuation to the flow is required. The larger flap angles are likely due to the increasing downwash at yaw. This is a promising result as it shows small actuation can be used at moderate yaw angles to achieve significant drag reduction, which is the conditions the vehicle will experience for the majority of its operation.

Figure 13 shows the sensitivity analysis for the cycle averaged drag design. The majority of the flaps show little to no sensitivity to changes. The greyed out repeatability interval is smaller for the cycle averaged drag as mentioned previously. Similar to the 0°-yaw optimised design, the cycle averaged optimised design shows sensitivity to the roof flaps, 4-6. Flaps 1 and 9 benefits from the opposite movement for the cycle averaged drag optimised design compared to the 0°-yaw optimised design. The −25° flap 1 and 9 for the 0°-yaw optimised design is expected to be separated and the wake plane supports this. This shows one of the benefits of considering several yaw angles to find drag sensitivities of surfaces which at 0°-yaw show no sensitivity to changes.

Flap sensitivity to drag was also analysed at yaw, Fig. 14. Some flaps, for example flap 12, show little or no change in drag when adding 2.5° or 5°. This is likely due to the flap being in separated flow at these high flap angles. Due to this, some of the flap angles in the optimised geometry have little impact on the overall performance.

4 Concluding Remarks

This work is focused on trailing edge flaps applied to a full-scale vehicle. The flap angles are optimised using a surrogate model-based algorithm to reduce drag at different yaw angles as well as reducing the cycle averaged drag, The flap angles are servo-controlled and are continually optimised while maintaining the wind speed. In total, almost 1500 designs were tested, resulting in approximately 40 hours of wind on time.

The cycle averaged drag optimised design is less sensitive to side wind compared to the 0°-yaw optimised design which shows a larger increase in drag for small yaw angles. The cycle averaged drag difference between the 0°-yaw optimised design and the cycle averaged drag optimised design are within the repeatability interval. However, the cycle averaged drag optimised design features significant reductions in lift. A slight upwash bias is introduced at 0°-yaw for the cycle averaged drag optimised design to counteract the increase in downwash as the vehicle is yawed. The cycle averaged drag optimised design outperforms the 0°-yaw optimised design at all yaw angles except 0°-yaw.

A 5°-yaw optimised design with asymmetric tapering reduced drag by 3% at yaw compared to the 0°-yaw optimised design, by balancing the wake evident by the more symmetric base pressure and reduction in crossflow in the near wake. The symmetric cycle averaged drag optimised design features a smaller improvement at 5°-yaw of 1%.

Declarations

References

Aeroprobe. Omniprobe, (2018) http://www.aeroprobe.com/omniprobe/
Ahmed, S. R., Ramm, G., Faltin, G.: Some salient features of the time-averaged ground vehicle wake. SAE International Congress and Exposition (1984). https://doi.org/10.4271/840300
Bates, S., Sienz, J., Toropov, V.: Formulation of the Optimal Latin Hypercube Design of Experiments Using a Permutation Genetic Algorithm, vol. 2011. (2004). https://doi.org/10.2514/6.2004-2011

Bonnavion, G., Cadot, O.: Unstable wake dynamics of rectangular flat-backed bluff bodies with inclination and ground proximity. J. Fluid Mech., 854:196–232, (2018). https://doi.org/10.1017/jfm.2018.630. https://www.cambridge.org/core/product/identifier/S0022112018006304/type/journal_article

Bonnavion, G., Cadot, O., Herbert, V., Parpais, S., Vigneron, R., Délery, J.: Asymmetry and global instability of real minivans' wake. J. Wind Eng. Indus. Aerodyn., 184:77–89, (2019). https://doi.org/10.1016/j.jweia.2018.11.006. https://linkinghub.elsevier.com/retrieve/pii/S0167610518307578

Cooper, K. R.: The effect of front-edge rounding and rear-edge shaping on the aerodynamic drag of bluff vehicles in ground proximity. In SAE International Congress and Exposition. SAE International, (1985). https://doi.org/10.4271/850288

Cooper, K. R.: Truck aerodynamics reborn - lessons from the past. In International Truck & Bus Meeting & Exhibition. SAE International, (2003). https://doi.org/10.4271/2003-01-3376

Duell, E. G., George, A. R.: Measurements in the Unsteady Near Wakes of Ground Vehicle Bodies. In SAE Tech. Pap. SAE International, (1993). https://doi.org/10.4271/930298. http://www.sae.org/technical/papers/930298

Evrard, A., Cadot, O., Herbert, V., Ricot, D., Vigneron, R., Délery, J.: Fluid force and symmetry breaking modes of a 3D bluff body with a base cavity. J. Fluids Struct., 61:99–114, (2016). https://doi.org/10.1016/j.jfluidstructs.2015.12.001. https://linkinghub.elsevier.com/retrieve/pii/S0889974615002698

Favre, T., Efraimsson, G.: An assessment of detached-eddy simulations of unsteady crosswind aerodynamics of road vehicles. Flow Turbul. Combust. **87**(1), 133–163 (2011). https://doi.org/10.1007/s10494-011-9333-4

Favre, T.: Aerodynamics simulations of ground vehicles in unsteady crosswind. KTH Royal Institute of Technology, Stockholm, (2011). http://urn.kb.se/resolve?urn=urn:nbn:se:kth:diva-50242. OCLC: 940898583

Garcia de la Cruz, J. M., Brackston, R. D., Morrison, J. F.: Adaptive base-flaps under variable cross-wind. (2017). https://doi.org/10.4271/2017-01-7000. http://www.sae.org/content/2017-01-7000/

Howell, J., Passmore, M., Tuplin, S.: Aerodynamic drag reduction on a simple car-like shape with rear upper body taper. SAE Int. J. Passeng. Cars Mech. Syst. **6**, 52–60 (2013). https://doi.org/10.4271/2013-01-0462

Howell, J.: Aerodynamic Drag of Passenger Cars at Yaw. SAE Int. J. Passeng. Cars Mech. Syst., 8(1), (2015). https://doi.org/10.4271/2015-01-1559. http://papers.sae.org/2015-01-1559/

Howell, J., Passmore, M., Windsor, S.: A drag coefficient for test cycle application. SAE Int. J. Passeng. Cars Mech. Syst., 11(5):447–461, (2018). https://doi.org/10.4271/2018-01-0742. https://www.sae.org/content/2018-01-0742/

Howell, J., Forbes, D., Passmore, M.: A drag coefficient for application to the WLTP driving cycle. Proceedings of the Institution of Mechanical Engineers, Part D: Journal of Automobile Engineering 231(9), 1274–1286 (2017). https://doi.org/10.1177/0954407017704784

J1594. Vehicle Aerodynamics Terminology (J1594 Ground Vehicle Standard) - SAE Mobilus. https://saemobilus.sae.org/content/j1594_199412

Josefsson, E., Hagvall, R., Urquhart, M., Sebben, S.: Numerical Analysis of Aerodynamic Impact on Passenger Vehicles during Cornering. (2018). https://doi.org/10.4271/2018-37-0014. http://www.sae.org/content/2018-37-0014/

Le Good, G., Resnick, M., Boardman, P., Clough, B.: Effects on the aerodynamic characteristics of vehicles in longitudinal proximity due to changes in style. (2018). https://doi.org/10.4271/2018-37-0018. https://www.sae.org/content/2018-37-0018/

Li, R., Borée, J., Noack, B.R., Cordier, L., Harambat, F.: Drag reduction mechanisms of a car model at moderate yaw by bi-frequency forcing. Phys. Rev. Fluids (2019). https://doi.org/10.1103/PhysRevFluids.4.034604

Ljungskog, E.: Evaluation and modeling of the flow in a slotted wall wind tunnel. Chalmers University of Technology, (2019). https://research.chalmers.se/en/publication/514006

Lorite-Díez, M., Jiménez-González, J. I., Pastur, L., Cadot, O., Martínez-Bazán, C.: Drag reduction on a three-dimensional blunt body with different rear cavities under cross-wind conditions. *J. Wind Eng. Indus. Aerodyn.*, 200:104145, (2020). https://doi.org/10.1016/j.jweia.2020.104145. https://www.sciencedirect.com/science/article/pii/S0167610520300556

Pavlovic, J., Marotta, A., and Ciuffo, B.: CO 2 emissions and energy demands of vehicles tested under the NEDC and the new WLTP type approval test procedures. Appl. Energy. 177:661–670, (2016). https://doi.org/10.1016/j.apenergy.2016.05.110. https://linkinghub.elsevier.com/retrieve/pii/S0306261916307152

Perry, A.-K., Pavia, G., Passmore, M.: Influence of short rear end tapers on the wake of a simplified square-back vehicle: wake topology and rear drag. 57(11):169. https://doi.org/10.1007/s00348-016-2260-3

Pfeiffer, J., King, R.: Robust control of drag and lateral dynamic response for road vehicles exposed to cross-wind gusts. Exp. Fluids **59**(3), 45 (2018). https://doi.org/10.1007/s00348-017-2479-7

Rao, A.N., Zhang, J., Minelli, G., Basara, B., Krajnović, S.: An LES investigation of the near-wake flow topology of a simplified heavy vehicle. Flow Turbul. Combust. **102**(2), 389–415 (2019). https://doi.org/10.1007/s10494-018-9959-6

Rossitto, G., Sicot, C., Ferrand, V., Borée, J., Harambat, F.: Aerodynamic performances of rounded fastback vehicle. Proceedings of the Institution of Mechanical Engineers, Part A: Journal of Power and Energy, pages 1211–1221, (2017). https://doi.org/10.1177/0954407016681684. https://hal.archives-ouvertes.fr/hal-01449542

SNIC. Swedish national infrastrucutre for computing, (2019). http://www.snic.se/

Schuetz, T. C.: Aerodynamics of Road Vehicles, Fifth Edition. SAE International, Warrendale, Pennsylvania, 5 edition edition, (2015)

Sterken, L., Löfdahl, L., Sebben, S., Walker, T.: Effect of rear-end extensions on the aerodynamic forces of an SUV. In SAE Technical Papers, (2014a). https://doi.org/10.4271/2014-01-0602. URL http://papers.sae.org/2014-01-0602/

Sterken, L., Sebben, S., Walker, T., Löfdahl, L.: Effect of the traversing unit on the flow structures behind a passenger vehicle. IMechE International Vehicle Aerodynamics Conference, (2014b). https://research.chalmers.se/en/publication/217295

Sternéus, J., Walker, T., Bender, T.: Upgrade of the volvo cars aerodynamic wind tunnel. In SAE World Congress & Exhibition. SAE International, (2007). https://doi.org/10.4271/2007-01-1043

Tunay, T., Firat, E., Sahin, B.: Experimental investigation of the flow around a simplified ground vehicle under effects of the steady crosswind. Int. J. Heat Fluid Flow, 71:137–152, (2018). https://doi.org/10.1016/j.ijheatfluidflow.2018.03.020. https://linkinghub.elsevier.com/retrieve/pii/S0142727X17308706

Urquhart, M., Ljungskog, E., Sebben, S.: Surrogate-based optimisation using adaptively scaled radial basis functions. Appl. Soft Comput. (2020). https://doi.org/10.1016/j.asoc.2019.106050

Urquhart, M., Varney, M., Sebben, S., Passmore, M.: Aerodynamic drag improvements on a square-back vehicle at yaw using a tapered cavity and asymmetric flaps. Int. J. Heat Fluid Flow, 86:108737, (2020a). https://doi.org/10.1016/j.ijheatfluidflow.2020.108737. http://www.sciencedirect.com/science/article/pii/S0142727X20305130

Urquhart, M., Sebben, S., Sterken, L.: Numerical analysis of a vehicle wake with tapered rear extensions under yaw conditions. J. Wind Eng. Indus. Aerodyn., 179:308–318, (2018). https://doi.org/10.1016/j.jweia.2018.06.001. https://www.sciencedirect.com/science/article/pii/S0167610518301144

Varney, M., Passmore, M., Gaylard, A.: Parametric Study of Asymmetric Side Tapering in Constant Cross Wind Conditions. SAE Int. J. Passeng. Cars - Mech. Syst. 11(3):213-224,, (2018). https://doi.org/10.4271/2018-01-0718. http://www.sae.org/content/2018-01-0718/

Varney, M.: Base drag reduction for squareback road vehicles. thesis, Loughborough University, (2020). https://repository.lboro.ac.uk/articles/Base_drag_reduction_for_squareback_road_vehicles/11823759

Wang, Y., Sicot, C., Borée, J., Grandemange, M.: Experimental study of wheel-vehicle aerodynamic interactions. J. Eng. Indus. Aerodyn., 198:104062, (2020). https://doi.org/10.1016/j.jweia.2019.104062. http://www.sciencedirect.com/science/article/pii/S0167610519306622

Wieser, D., Nayeri, C. N., Paschereit, C. O.: Wake structures and surface patterns of the DrivAer notchback car model under side wind conditions. Energies, 13(2):320, (2020). https://doi.org/10.3390/en13020320. https://www.mdpi.com/1996-1073/13/2/320

Windsor, S.: Real world drag coefficient - is it wind averaged drag? In Int. Veh. Aerodyn. Conf., 3–17. Elsevier, (2014). https://doi.org/10.1533/9780081002452.1.3. https://linkinghub.elsevier.com/retrieve/pii/B9780081001998500010